Quasi-freestanding graphene on SiC(0001) via cobalt intercalation of zero-layer graphene

A. A. Rybkina [1,*] S. O. Filnov [1] A. V. Tarasov [1] D. V. Danilov,[1] M. V. Likholetova,[1] V. Yu. Voroshnin,[1,2] D. A. Pudikov,[1]
D. A. Glazkova,[1] A. V. Eryzhenkov [1] I. A. Eliseyev,[3] V. Yu. Davydov [3] A. M. Shikin,[1] and A. G. Rybkin [1]

[1]*Saint Petersburg State University, 198504 Saint Petersburg, Russia*
[2]*Helmholtz-Zentrum Berlin für Materialien und Energie, Elektronenspeicherring BESSY II,*
Albert-Einstein-Str. 15, D-12489 Berlin, Germany
[3]*Ioffe Institute, 194021 Saint Petersburg, Russia*

Modification of the electronic and crystal structure of zero-layer graphene grown on 6*H*-SiC(0001) after Co intercalation is reported. Using a wide range of techniques including angle-resolved photoelectron spectroscopy, x-ray photoelectron spectroscopy, Raman spectroscopy, low-energy electron diffraction, we found that zero-layer graphene on SiC transforms into graphene monolayer as a result of cobalt intercalation. The Dirac cone of π band characteristic of quasi-freestanding graphene is observed. In combination with high-resolution transmission electron microscopy and atomic force microscopy data, we conclude that ultrathin silicide CoSi/CoSi$_2$ structure is formed between graphene and SiC substrate. Investigation of magnetic properties reveals ferromagnetic behavior with open hysteresis loop. The results of this work are the basis for further implementation of magneto-spin-orbit graphene on a semiconducting substrate and are important for the future application of such graphene in spintronics.

I. INTRODUCTION

Graphene remains to be one of the promising materials in modern condensed matter physics. Linear dispersion dependence $E(k)$ provides an unusually high conductivity of electrons because of ballistic transport and many other unique electronic properties [1,2]. Being a nonmagnetic material with a weak spin-orbit interaction, graphene cannot be considered as an active element of spintronics. However, the giant spin splitting of electronic states observed in graphene upon contact with heavy and magnetic metals opens up broad prospects for use in spintronic devices, in particular, in the field of information storage and quantum computing [3–5]. One of the most anticipated realization of graphene in spintronics is magneto-spin-orbit graphene [3] which consists of well-ordered graphene upon contact with the strong ferromagnetic element (cobalt) and the heavy metal (gold or platinum). When interacting with cobalt and gold, graphene not only retains its unique characteristics but also partially adopts the properties of these metals—magnetism and spin-orbit interaction. For successful application of graphene in device elements, it is necessary to use insulating substrates. The silicon carbide (SiC) is one of the most promising semiconductor substrates for formation of thin nanosystems based on epitaxial graphene [6,7]. Thereby realization of magneto-spin-orbit graphene on SiC substrate is an actual challenge.

For this aim, the magnetic and heavy atoms should be intercalated underneath graphene on SiC to provide the required properties. Nevertheless, it should be noted that there is an additional interface carbon layer between graphene and

SiC substrate—a zero-layer graphene (ZLG). So in many cases, intercalation of foreign atoms occurs below or between these carbon layers [8–11]. Therefore, to obtain an intercalated single-layer graphene, it is necessary to intercalate the magnetic atoms below ZLG on SiC substrate. Studying the functionalization methods of ZLG on SiC substrate is an important area, since it will allow creating of layered structures based on a graphene monolayer atop of semiconductor substrate and impart the unique properties to it. Intercalation of magnetic metals under ZLG will make it possible to create single-layered graphene coatings on the magnetic metal intercalate. Intercalation underneath a zero-layer graphene on SiC was investigated previously for Sb [12], Ge [13], Bi [14], Cu [15], and Si [16]. In these references, the transformation of ZLG into a single-layer graphene has been observed. Recently, the Co intercalation underneath ZLG was studied [17], self-limited silicide formation was reported followed by Co intercalation between graphene and silicide.

In this work, we will try to explain the process that takes place at the initial stage of Co intercalation, since a question about modification of the graphene electronic structure under intercalation of ultrathin layer of Co still remains unresolved. It should be noted that ARPES and Raman spectroscopy data were not shown previously on Co intercalation under ZLG/SiC and the formation of quasi-freestanding graphene was not proven yet. Moreover, it is very exciting to investigate the graphene properties on the magnetic ultra-thin silicide layer, as it is known that cobalt silicides exhibit various magnetic properties, from antiferromagnetic and ferromagnetic to paramagnetic behavior, depending on the stoichiometry, the quality of crystal structure and the temperature of formation [18,19]. Various Hall effects driven by spin-orbit and magnetic proximity coupling are predicted in graphene, such

———————
*a.rybkina@spbu.ru

as quantum-anomalous Hall effect (QAHE), valley-polarized QAHE, quantum valley Hall effect, and circular dichroism Hall effect [20,21].

II. METHODS

Synthesis and photoemission experiments were carried out *in situ* under ultrahigh vacuum conditions in the photoemission spectroscopy setup Univer-M at the Resource Center "Physical Methods of Surface Investigation" of Saint Petersburg State University Research park (SPbU Research park). The samples were investigated by x-ray photoelectron spectroscopy (XPS), angle-resolved photoelectron spectroscopy (ARPES) using a VG Scienta R4000 hemispherical energy analyzer. A narrow-band high-intensity source of ultraviolet radiation VUV 5k with a monochromator and an x-ray radiation source with an Al anode were used as excitation source. The photoelectron spectra of the core levels were deconvoluted into spectral components by fitting procedure. The line shape of Si $2p$ and C $1s$ spectra was defined by Gaussian/Lorentzian product formula with mixing parameters of 0.5 and 0.9, respectively [22,23]. The asymmetry parameter for the graphene peak of C $1s$ spectra was 0.12. The details of the fitting procedure for C $1s$ core level spectra are presented in Ref. [24] (see, also, Refs. [25–28] therein). Accurate peak fitting of the Co $2p$ spectrum obtained with Al Kα radiation is made in accordance with Ref. [29]. Raw data are shown in figures by circles along with the best-fit spectra, the corresponding components, and the background.

The n-type and semi-insulating wafers of $6H$-SiC(0001) purchased from TankeBlue Semiconductor Co. Ltd. were used in the experiment. The amount of deposited cobalt layers was controlled with a quartz microbalance and varied in the range from 4 to 20 Å. The sample temperature was determined using Keller CellaTemp PA 20 AF 2/C pyrometer with the emissivity set to 0.6 for 60° off-normal angle.

Low-energy electron diffraction (LEED), atomic force microscopy (AFM) and Raman spectroscopy were used to analyze the surface structure. AFM measurements were carried out under atmospheric conditions and at room temperature in the tapping mode on a NT-MDT Solver Pro-M microscope. The Raman spectra were obtained at room temperature using a Horiba Jobin-Yvon T64000 setup equipped with a confocal optical microscope. A solid-state Nd:YAG laser with a wavelength of 532 nm served as an excitation source. The laser beam was focused on the sample using a 100× objective lens (NA = 0.9) into a spot ~1 μm in diameter. To avoid damaging the sample, the laser beam power was limited to 4.0 mW.

High-resolution transmission electron microscopy (HRTEM) measurements were performed with the use of Zeiss Libra 200FE microscope equipped with detectors of high-angle annular dark-field scanning transmission electron microscopy (HAADF-STEM) and energy-dispersive x-ray spectroscopy (EDX) at the Interdisciplinary Resource Centre for Nanotechnology of SPbU Research park. The accelerating voltage of 200 kV was set for measurements. Sample preparation was carried out using a lift-out technique in a Zeiss Auriga focused ion beam scanning electron

microscope (FIB-SEM). PtC amorphous capping material was deposited to prevent the damage to the top surface during FIB processing.

Measurements of magnetic properties were carried out at the Resource Center "Center for Diagnostics of Materials for Medicine, Pharmacology, and Nanoelectronics" of SPbU Research park using a SQUID magnetometer with a helium cryostat manufactured by Quantum Design. The experiments were performed in a pull mode in terms of temperature and magnetic field. The magnetic measurements were carried out by applying the magnetic field parallel to the surface ($\perp$ c axis).

First-principles calculations in the framework of the density functional theory (DFT) were performed at the Computing Center of SPbU Research park. The band structure calculations were conducted within the pseudopotential localized pseudoatomic orbital basis approach, as implemented in the OPENMX software package [30,31]. The basis set used in our work contains five basis functions (s2p2d1) for C and Si atoms as well as three basis functions (s2p1) for H atom, which is sufficient for accurate description of the electronic structure. To describe the exchange-correlation energy, we applied the generalized gradient approximation (GGA) using the Perdew-Burke-Ernzerhof exchange-correlation potential [32]. Because the inclusion of the full symmetry of the silicon carbide substrate and graphene, as in the $(6\sqrt{3}\times6\sqrt{3})$R30° reconstruction, would require the use of 1648 atoms [33], we used the most stable structure of the $(\sqrt{3}\times\sqrt{3})$R30° SiC reconstruction, which can capture the most important features of zero-layer graphene [34]. We constructed the model of SiC substrate with six SiC layers, which was utilized to deposit a 32 atom 4×4 graphene unit cell. The C terminated side was saturated with H atoms. For the self-consistent field (SCF) cycle, a k-point grid of 3×3×1 was used to sample the Brillouin zone (BZ) of the unit cell. The band structure unfolding from a supercell to a primitive cell BZ of zero-layer graphene was performed according to Ref. [35]. The structural optimization was done using the full potential (FP) "augmented-plane-wave+local orbitals" method (APW+lo) [36] implemented in WIEN2K code [37]. The parameter determining the accuracy of the calculations within the APW + lo method, RMT × K_{max} was set to 3.0, where RMT is the smallest atomic sphere radius and is the plane wave basis set cutoff. The atomic sphere radii were set to 1.65 a_0 for silicon, 1.34 a_0 for carbon, and 0.72 a_0 for hydrogen, where a_0 is a Bohr radius. The atomic positions in each unit cell were relaxed within the scalar relativistic approximation until the forces on each atom were less than 1 mRy/bohr (3×10^{-2} eV/Å).

III. RESULTS AND DISCUSSION

A. Zero-layer graphene on $6H$-SiC(0001)

The well-established approach of graphene synthesis is thermal graphitization of SiC surfaces under ultrahigh vacuum (UHV) conditions [7,38–43]. Prior to graphitization process, several atomic reconstructions of SiC surface can be obtained: (3×3), $(\sqrt{3}\times\sqrt{3})$R30°, and $(6\sqrt{3}\times6\sqrt{3})$R30°. For synthesis of the intercalated graphene monolayer on SiC, it is more
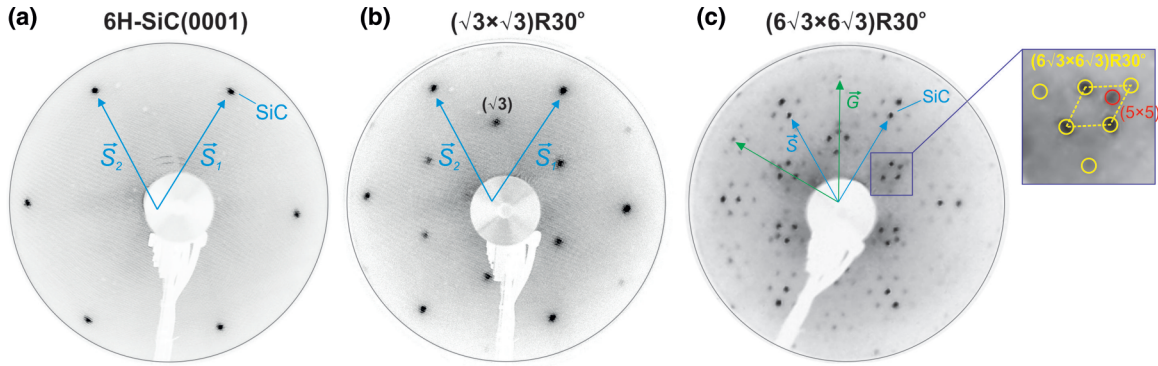
FIG. 1. LEED patterns of (a) initial surface of 6H-SiC(0001), $E_p = 50$ eV, (b) ($\sqrt{3} \times \sqrt{3}$)R30° reconstruction of SiC surface after annealing at temperature of 950 °C, $E_p = 57$ eV, and (c) (6$\sqrt{3} \times 6\sqrt{3}$)R30° reconstruction of SiC surface (zero-layer graphene) after annealing at temperature of 1150 °C, $E_p = 89$ eV.

appropriate to use (6$\sqrt{3} \times 6\sqrt{3}$)R30° reconstruction of SiC, that is called a ZLG. It is a carbon layer with graphene-like hexagonal arrangement but about 1/3 of these carbon atoms are covalently bonded with Si atoms of the SiC substrate [38,39]. As the result, no linear dispersion of the π band typical for the graphene Dirac cone can be detected in the electronic structure of ZLG.

The method of high-temperature annealing of 6H-SiC(0001) surface was employed for ZLG synthesis [43]. The first step is degassing of the sample in UHV at around 600 °C. Every annealing step is limited by 15 min. Figure 1(a) shows the bright LEED patters of (1×1) structure with reciprocal vectors ($s1$, $s2$) for the clean surface of SiC(0001). The same LEED image is observed for annealing at temperatures below 900 °C. Next step of annealing between 970 °C and 1100 °C leads to formation of the ($\sqrt{3} \times \sqrt{3}$)R30° structure of SiC [see diffraction pattern in Fig. 1(b)]. Such a wide range of temperatures is due to the averaging of data for several samples. At around 1150 °C the reconstructions "($\sqrt{3}$)" and "($6\sqrt{3}$)" coexist. Finally, annealing at $T = 1150$-1170 °C reveals a (6$\sqrt{3} \times 6\sqrt{3}$)R30° structure or ZLG on SiC. The typical LEED pattern of ZLG on SiC is presented in Fig. 1(c) [7,38–43]. The homogeneous LEED pattern of ZLG is observed throughout the sample.

Step by step high-temperature annealing in UHV chamber allows us to define the accurate parameters to reach high-quality ZLG on SiC by analyzing LEED, XPS, and ARPES data obtained *in situ*. After that it is possible to synthesize ZLG on SiC by one-step high-temperature annealing at 1150 °C with preliminary degassing of the sample.

One of the distinctive features of LEED pattern for ZLG is the evolution of the reflexes inside the rhombus marked by yellow dash line on Fig. 1(c) [39–41,43]. At $T = 1150$ °C there are two reflexes inside the rhombus, and the structures "($\sqrt{3}$)" and "($6\sqrt{3}$)" coexist. The first reflex (in the lower half of the rhombus) corresponds to the ($\sqrt{3} \times \sqrt{3}$)R30° structure and the other one (in the upper half of the rhombus)-the quasi (5×5) structure, that is connected with the (6$\sqrt{3} \times 6\sqrt{3}$)R30° reconstruction [41]. At $T = 1150$ °C–1170 °C only one bright reflex in the upper half of the rhombus remains [Fig. 1(c)] that corresponds to ZLG formation on the surface [39,41].

The valence band of synthesized ZLG on SiC is measured by ARPES mapping in a wide range of binding energy and momentum. In Figs. 2(a)–2(e), the electronic structure of ZLG on 6H-SiC(0001) measured along and orthogonal to the $\overline{\Gamma K}$ direction of the surface BZ is shown. Typical for graphene π states do not contribute to the band structure, while the clear graphene-like σ states are resolved. A strong hybridization of ZLG electronic states with the states of SiC-substrate can be distinguished below the 3 eV of binding energies that leads to the avoided-crossing effects and energy gaps in the crossing points. Other distinctive features of ZLG are the two localized states $g1$ and $g2$ at binding energies of 0.4 and 1.6 eV that are observed near the Fermi level [16,38,42,44]. To verify our ARPES data measured at photon energy of 40.8 eV, the first-principles calculations in the framework of the density functional theory (DFT) were performed for the relaxed unit cell [Figs. 2(g) and 2(h)]. Despite the fact that similar calculations have already been published earlier [45,46], the band structure calculated for the wide energy range of 0–17 eV is presented here for the first time. Calculation results show that the graphene Dirac cone band dispersion is indeed absent, leaving a large band gap of 1.5 eV and strong n-doping state caused by the strong covalent bonding between ZLG and the Si atoms of the SiC substrate. The flat band just below the Fermi level is due to the unsaturated Si dangling bonds at the interface [45]. For easy reference, when comparing the ARPES data with the calculated band structure [Figs. 2(g) and 2(h)] we marked the main features $\boxed{1}$, $\boxed{2}$, $\boxed{3}$ that have a clear coincidence. Of particular interest is the presence of the energy gaps in the crossing points of graphene σ and substrate states in the 6–10 eV energy region both in theory and experiment that indicate interaction between them [denoted by dashed rectangle in Figs. 2(d) and 2(g)].

XPS data analysis also supports our conclusion of successful ZLG synthesis. Figure 3(a) shows the XPS spectrum of C 1s for ZLG on SiC(0001), the characteristic shape of which is explained by the presence of three components: peak at 283.6 eV corresponds to carbon atoms in SiC, and two components S1 (284.7 eV) and S2 (285.5 eV) correspond to carbon atoms in ZLG [17,38,39]. Component S2 is related to the in-plane bonding of the reconstructed layer and component S1 is due to the out-of-plane bonding of the reconstructed layer to the topmost Si atoms of the substrate.
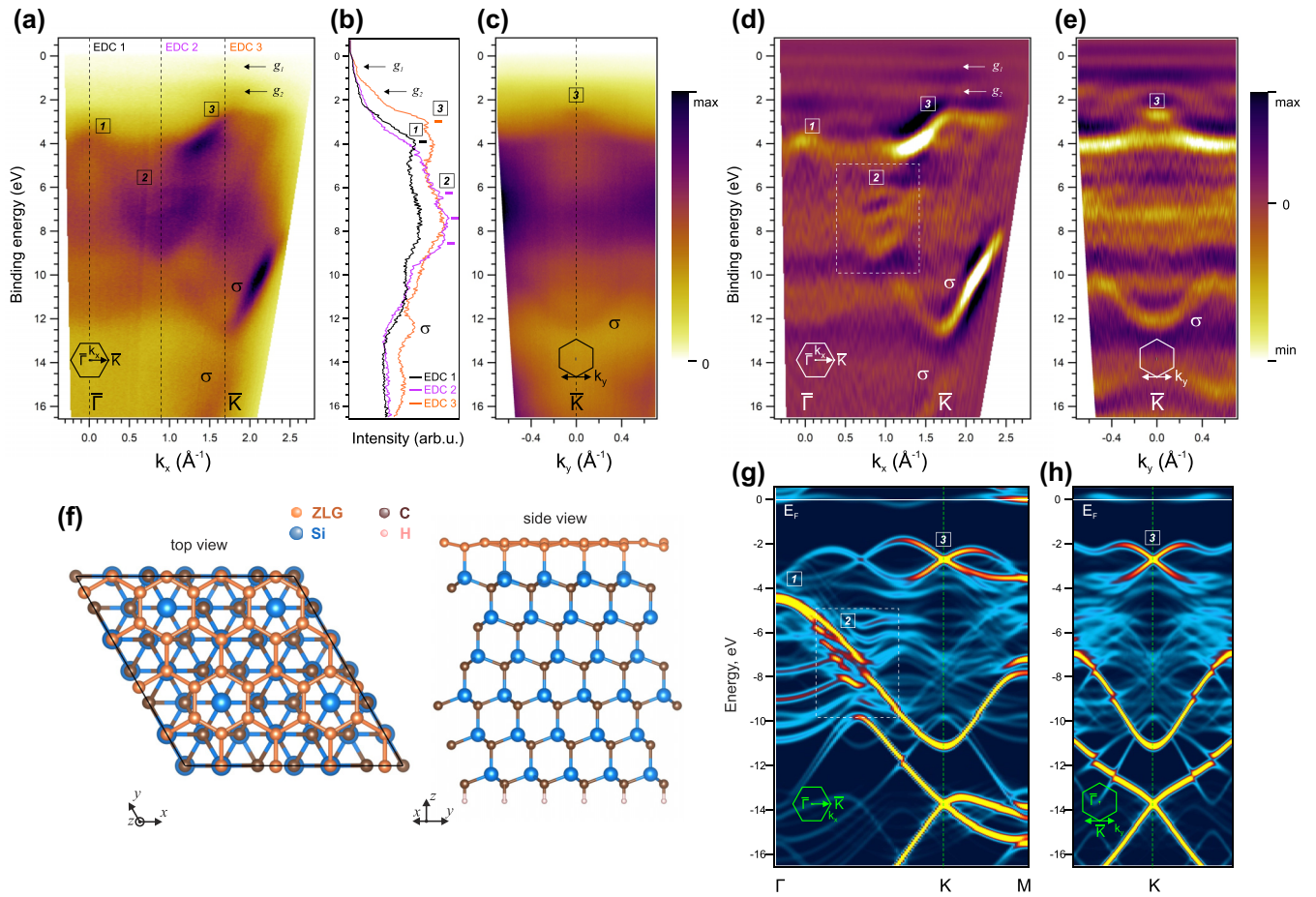
FIG. 2. [(a) and (c)] ARPES intensity maps of ZLG on 6*H*-SiC(0001) measured in the direction along and orthogonal to the $\overline{\Gamma K}$ direction of the surface BZ, the photon energy is 40.8 eV (HeIIα). (b) Energy distribution curves (EDC) for momenta along cuts indicated in (a). [(d) and (e)] ARPES data presented as the second derivative by energy to discern the main features more clearly. (f) Ball-and-stick model of ZLG arrangement on top of 6*H*-SiC(0001) substrate. [(g) and (h)] Calculated band structure of ZLG on 6*H*-SiC(0001) in the direction along and orthogonal to the $\overline{\Gamma K}$ direction in the same energy range.

B. Deposition of Co on "cold" and "heated" substrates

To select the most optimal mode, Co intercalation under ZLG was carried out in two ways. In the first stage (I), 10 Å of cobalt were deposited on the substrate at room temperature

with subsequent annealing during 3 hours at temperature of 550 °C. Since ZLG intercalation was incomplete under these conditions, in the second stage (II), 14 Å of Co were deposited during ~1.5 hours on the heated substrate at 450 °C.
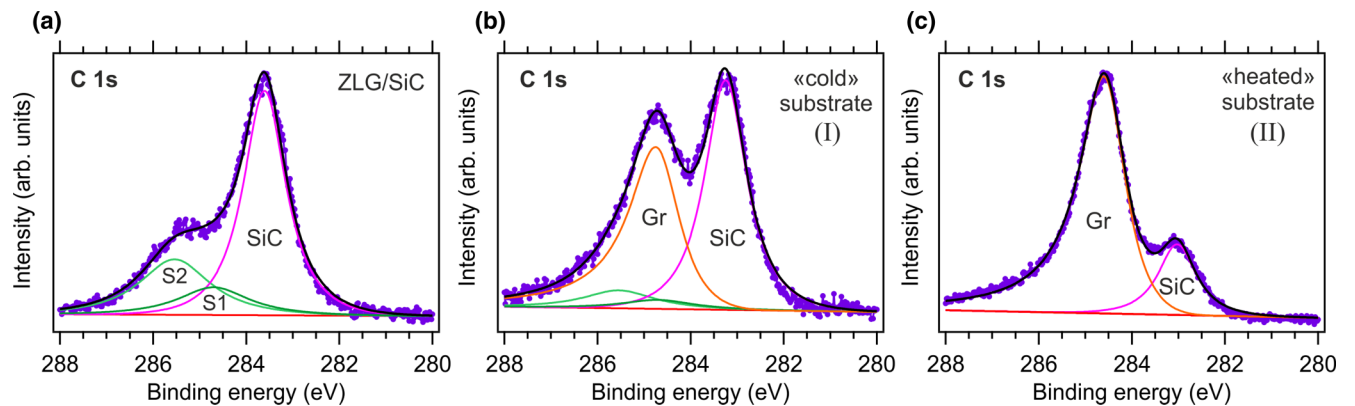

FIG. 3. XPS spectra of C 1*s* core level for (a) ZLG on 6*H*-SiC(0001), (b) after intercalation of 10 Å Co by deposition on the substrate at room temperature with subsequent annealing (stage I), and (c) after intercalation of 14 Å Co by deposition on the heated substrate (stage II). The photon energy is 1486.6 eV. All spectra are normalized on the maximum of intensity.

Figures [3(b)] and [3(c)] show the C 1*s* photoelectron spectra measured after two intercalation stages. Upon intercalation of Co under ZLG on SiC, the S1, S2, and the SiC spectral components decrease in intensity. A new peak (Gr) appears at the binding energy of 284.6–284.8 eV, which is characteristic for graphene [10,38,39]. The intensity of graphene component is significantly higher after additional intercalation on the heated substrate. It indicates a larger-scale coverage of the surface with graphene monolayer [Fig. 3(c)], while for the stage (I) [Fig. 3(b)], the phases of ZLG and graphene coexist on the surface and the complete transformation of ZLG into the graphene monolayer cannot be reached. The LEED image accompanying the stage (I) in Fig. 3(b) shows that reflexes of ZLG and graphene coexist (see Sec. II in Ref. [24]). Moreover, the intensities of graphene and S1, S2 components were analyzed after 10 Å Co deposition and intercalation by two described methods on different samples (see Sec. II in Ref. [24]). It claims that transformation of ZLG into the graphene monolayer occurs ∼1.4 times more efficiently in case of cobalt deposition on the heated substrate than in case of cobalt deposition at room-temperature substrate with subsequent annealing. The efficiency of intercalation during metal deposition on the heated substrate was previously shown for graphene/SiC system [47], but this finding for intercalation underneath ZLG/SiC is reported for the first time.

C. Quasi-freestanding graphene by Co intercalation

Based on the results of the previous section, we intercalated cobalt on the heated substrate. For this purpose, 20 Å of Co were deposited during 1 hour on ZLG/SiC substrate heated at 450 °C. Under these conditions, Co intercalation occurred directly during the deposition of metal atoms.

1. XPS data analysis

In Fig. 4, the changes in the XPS spectra of C 1*s* and Si 2*p* core levels after cobalt intercalation are shown. Deconvolution of the photoelectron spectra into components by a fitting procedure is presented. The C 1*s* spectrum of ZLG on SiC has a characteristic shape, as described in the text for Fig. 3(a). For this sample, three components are also detected: two components S1 (284.60 eV) and S2 (285.45 eV), corresponding to the carbon in ZLG, and the component of bulk carbon in the SiC compound (283.69 eV). The Si 2*p* spectrum [Fig. 4(b)] represents one broad peak at the binding energy of 101.66 eV with a full width at half maximum (FWHM) equal to 1.4 eV, which is in accordance with the previous results [17,39,41,43,44,48,49]. However, the Si spin-orbit coupling doublet ($2p_{1/2}$ and $2p_{3/2}$) is not resolved in case of using an Al-anode x-ray tube, so the one asymmetric peak is obtained in the spectrum. The asymmetry parameter and the width of the bulk Si 2*p* component were kept fixed for all fitting procedures.

The shape of C 1*s* and Si 2*p* spectra in Fig. 4 changes after 20 Å Co intercalation at sample temperature of 450 °C. S1 and S2 components are no longer visible in the C 1*s* spectrum, but an intense component corresponding to graphene appears at the binding energy of 284.4 eV [10,38,39]. The shape of Si 2*p*
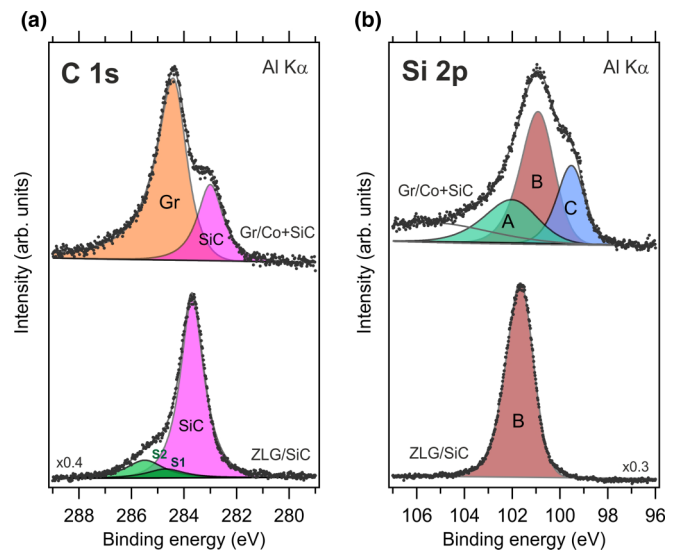

FIG. 4. XPS spectra of C 1*s* (a) and Si 2*p* (b) core levels measured for ZLG on SiC (bottom row) and after 20 Å Co intercalation underneath ZLG on SiC (top row). The photon energy is 1486.6 eV.

spectrum provides important information about the processes occurred. After intercalation of cobalt, the Si 2*p* spectrum already has a complex multi-component shape (Fig. 4). In addition to the main bulk component in Si 2*p* spectrum, two new components appear to the right and left of the main peak. A component (A) at 102 eV is located at higher binding energies relative to the bulk component and may be related to the CoSi compound. The presence of a high-energy component relative to the bulk component in the Si 2*p* spectrum corresponding to the CoSi compound was also noted in Refs. [10,50]. The low-energy component (C) at the binding energy of 99.5 eV can be attributed to the $CoSi_2$ compound with a lower Co concentration [50]. There are considerable contradictions in the published works regarding the energy position of Si 2*p* components in Co-Si compounds [10,49–52]. This is primarily due to the sensitivity of Co-Si compounds to the synthesis conditions: the amount of cobalt, the reaction temperature, and the crystal structure of the substrate surface. Therefore, for interpreting Si 2*p* components, we use several experimental methods, including angle-resolved XPS and Raman spectroscopy, and also check the data agreement with the cited references. The spectral components corresponding to Si and C atoms in the bulk SiC [denoted by (B) and (SiC) in Fig. 4] are both shifted by 0.7 eV towards lower binding energies. This effect can be explained by different surface band bending for cobalt silicide formed on top of SiC [53].

Thus, based on the XPS data, it can be concluded that cobalt atoms interact with the substrate during intercalation and two surface Co-Si compounds are formed, which are close in stoichiometry to the CoSi and $CoSi_2$.

However, to study the localization of the underlying layers, it is necessary to carry out additional analysis of the XPS data with angular resolution, in which photoelectron spectra are taken at different angles of emission. Analyzing the angular dependences of XPS core level intensities of the elements, it is possible to determine the relative positions of the layers in depth (see, for example, Supplemental Material of Ref. [54]).
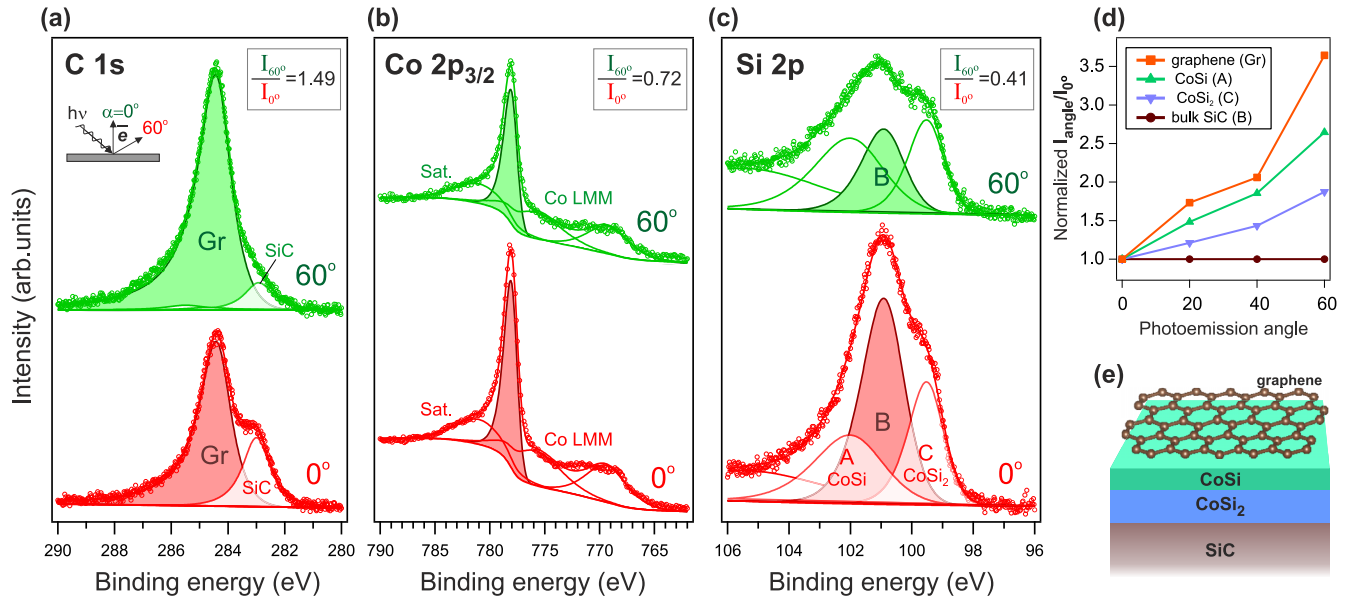
FIG. 5. Angle-resolved XPS spectra measured at emission angles of $0°$ and $60°$ relative to the surface normal for (a) C $1s$, (b) Co $2p$, (c) Si $2p$ core levels, after Co intercalation underneath ZLG on SiC. The photon energy is 1486.6 eV. (d) The $I_{angle}/I_{0°}$ intensity ratios of selected components, normalized by the Si $2p$ bulk component, depending on the photoemission angle. (e) The structure model of near-surface layers after Co intercalation based on angle-resolved XPS spectra analysis, it is not drawn to scale.

The experimental data of angle-resolved XPS are shown in Fig. 5. Figures 5(a)–5(c) shows the changes in the C $1s$, Co $2p$, and Si $2p$ spectra measured at photoemission angles of $0°$ and $60°$ relative to the surface normal. The intensity ratios of the selected components for these two angles gives us an understanding of the relative depth location. A larger photoemission angle gives us a more surface-sensitive spectrum. Therefore, comparing the $I_{60°}/I_{0°}$ intensity ratios for the C $1s$ graphene component, Co $2p_{3/2}$ main component and Si $2p$ bulk component (the numerical values of the ratios are shown in Figs. 5(a)–5(c) in the insets), we conclude that graphene is located above the cobalt silicides, while the latter are localized between graphene and SiC substrate. It proves the intercalation of Co underneath ZLG on SiC.

In Fig. 5(d), the values of $I_{angle}/I_{0°}$ ratios for more angles and for main components of the Si $2p$ spectrum are shown. In order to avoid the change in the x-ray radiation density in the analysis area with a change of the photoemission angle, we normalized the intensity of all components at a given angle to the intensity of the Si $2p$ bulk component at this angle. The intensity of the bulk component remains constant for all angles after normalization, and the fastest growing component belongs to the overlying layer, while the slowly growing - to the underlying layer. It is clearly visible that intercalation of Co leads to formation of the near-surface Co-Si alloys. According to Ref. [55], the formation of CoSi alloy on Si(100) surface takes place after annealing at $450°C$, and then, $CoSi_2$ phase is formed at the triple points of the two CoSi grains and the silicon surface with the increase of annealing temperature. It agrees well with our experimental data, which show CoSi compound directly underneath graphene and $CoSi_2$ compound below. In Fig. 5(e), a schematic structure model of the underlying layers after Co intercalation is presented, considering them as flat and having a homogeneous composition. The supposed model gives us information on

the process of cobalt intercalation and on the formed Co-Si compounds.

2. HRTEM and AFM study

To obtain information about the crystal structure of CoSi and $CoSi_2$ layers in detail, the HAADF-STEM and HRTEM measurements were performed. Figures 6(a) and 6(b) show Z contrast of the surface cross-section cut. The intermediate layer between SiC substrate and PtC capping layer has predominant thicknesses ranging from ~ 4 to ~ 10 nm. EDX profile proves the presence of Co atoms in this layer and decrease of Si atoms concentration from the SiC substrate to the capping layer. TEM and HRTEM images [Figs. 6(c)–6(e)] have an inverse contrast compared to the HAADF-STEM images. An enlarged view of the layer structure is presented on Fig. 6(d). Nanometer range steps between different lateral structures are well-resolved. The smallest interlayer spacing observed in HRTEM images is ~ 1.7 Å that coincides with STM measured height of each CoSi layer [56], while structure underneath has a higher interlayer spacing of ~ 2.1 Å. Zone axis search in the $40°$ angle range of sample rotation around the normal allows us to find the second zone axis which is $15°$ away from the first one. For the second zone axis [Fig. 6(e)], SiC unit cell is well-resolved, and the structure of the buried cluster is reproduced with $CoSi_2$ single crystal structure. We associate clusters formed at the interface with $CoSi_2$ covered by residual CoSi layer. The growth mechanism has similar behavior as for high-temperature $CoSi_2$ formation on Si(100) wafers when $CoSi_2$ starts to form at the interface of CoSi and Si [55,57,58]. Notably, that orientations of $CoSi_2$ clusters relative to the substrate differs on the panels (d) and (e) of Fig. 6 by $90°$ rotation (follow the rotation of $CoSi_2$ [222] vector shown in the figure). It means that different crystal growth directions of $CoSi_2$ are possible.
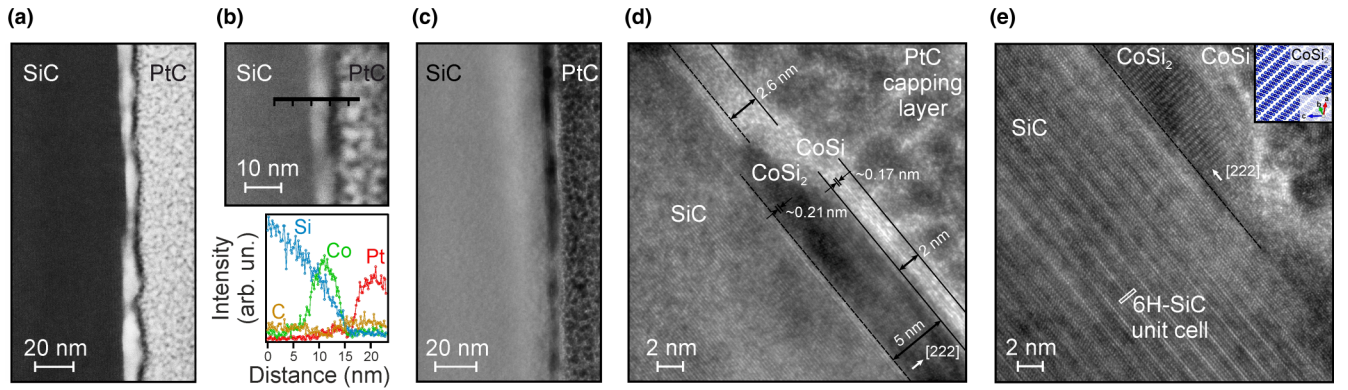
FIG. 6. [(a) and (b)] Cross-sectional HAADF-STEM images with EDX profile measured along the black line shown on (b). (c) Cross-sectional TEM image. [(d) and (e)] Cross-sectional HRTEM images measured for two different rotation angles around the surface normal ($0°$ and $15°$, correspondingly). The inset in (e) includes the cut of $CoSi_2$ single crystal structure for the reference.

The atomic structure of the CoSi layer is poorly resolved in HRTEM, and together with the absence of LEED diffraction spots these data indicate a misorientation in the atomic CoSi layers.

The surface topography of the same sample was measured by AFM. Figure 7(a) demonstrates the topography of the sample region covered with a metal mounting part. Figure 7(b) shows surface topography of the central region after Co intercalation. In the inserts on the right, one can see enlarged areas of AFM images as well as profiles along the red lines. The covered region presents a stepped surface, typical for annealed SiC [59] with many defects that are possibly connected with micropipes formation [60–62]. ZLG growth and Co intercalation result in a layered structure strewed by triangle clusters, with sizes about 5–10 nm. In Ref. [56], it was reported that the Co deposition on Si(111) surface leads to formation of $CoSi_x$ ($x = 1, 2$) islands with approximately triangular shape. Here, based on our experimental data, we also suggest formation of the triangular shape clusters with layered $CoSi_x$ structure.

3. ARPES and Raman spectroscopy study

ARPES study of ZLG on SiC after Co intercalation shows that ZLG transforms into graphene monolayer with formation of the linear Dirac cone in the region of the $\overline{K}$ point of the surface BZ [Figs. 8(a) and 8(b)]. The ARPES data in the $\overline{\Gamma K}$ direction are presented in Sec. III in Ref. [24] (see, also, Refs. [63,64] therein). The Dirac point is located at the binding energy of 0.35 eV below the Fermi level. A similar electronic structure of quasi-freestanding graphene was observed after intercalation of Si underneath graphene on Co or Ni substrates [65,66]. Nevertheless, we observe hybridization of graphene π states with the state at ~2.8 eV. This state can be related to CoSi compound according to calculated bulk density of states [67] and ARPES experiment [68]. In Fig. 8(c), the LEED pattern of ZLG after Co intercalation shows graphene (1×1) structure. Our theoretical DFT calculations confirm that graphene lies on the CoSi layer and show that quasi-freestanding graphene with a linear Dirac cone is possible only in the case of graphene on the CoSi surface. Meanwhile, in the case of graphene on $CoSi_2$, nearly ideal-like Dirac cone should be destroyed. This excludes the

possibility of significant contributions from in-plane domains of CoSi and $CoSi_2$ within the same layer under graphene. The corresponding DFT results and their description are presented in Sec. IV in Ref. [24].

Analysis of the Raman spectroscopy data allows one to obtain information on the sample's composition and crystal structure. The Raman spectra were measured in two different regions of the sample prepared by two-stage approach (Sec. III B): the central region in which ZLG growth and Co intercalation occurred, and the region that was covered with metal mounting part during sample processing. Figure 9(a) shows typical Raman spectra of these two regions. The
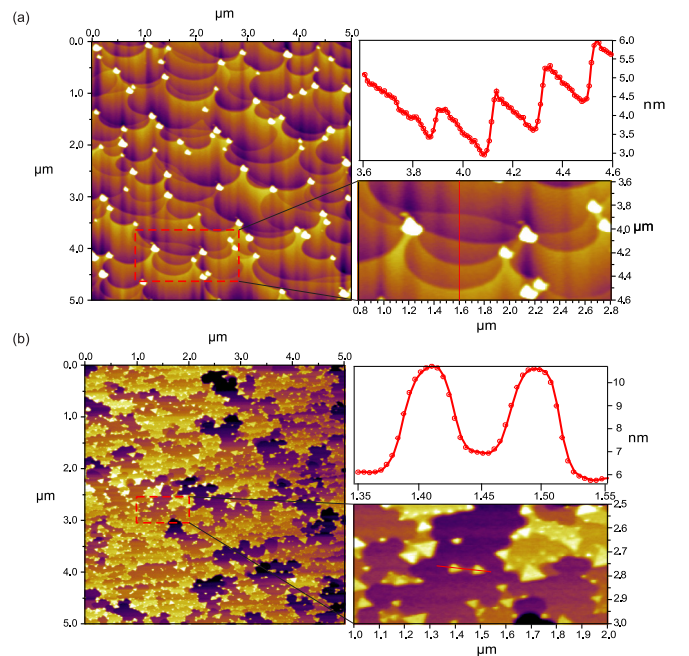

FIG. 7. $(5\times5)\mu$m AFM images of the surface of covered 6H-SiC(0001) (a) and the surface of 6H-SiC(0001) after ZLG growth and Co intercalation (b). Enlarged scale images are shown on the right part. The profiles taken along the red lines on the scaled images are presented in the upper part of the figures.
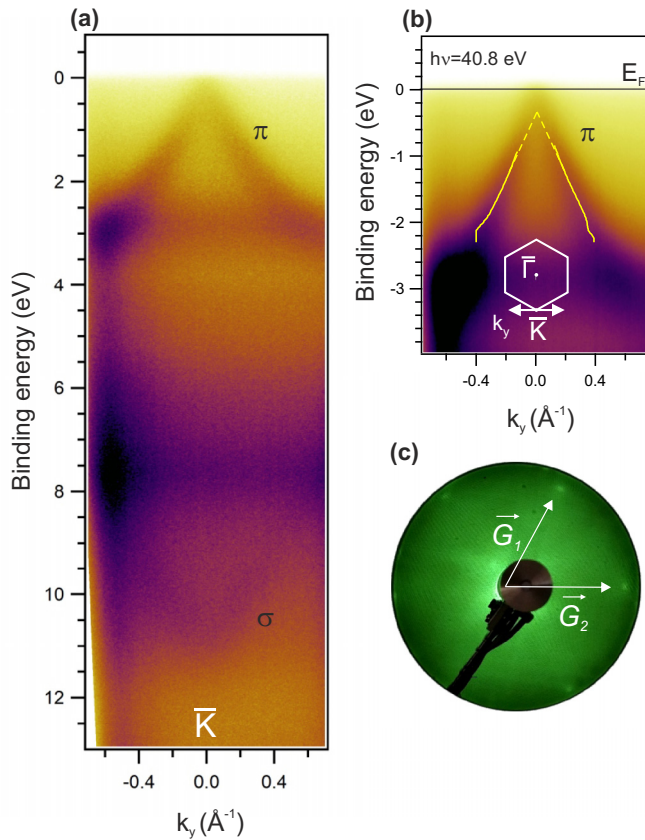
FIG. 8. (a) ARPES intensity map for π band of Co-intercalated ZLG/SiC measured in the direction orthogonal to the $\overline{\Gamma K}$. ARPES data were measured at the photon energy of 40.8 eV (HeIIα) and at room temperature of the sample. (b) The Dirac cone of the quasi-freestanding graphene after Co intercalation. Solid yellow lines show the result of momentum distribution curves fitting with two Lorentzian peak functions. (c) LEED pattern of Co-intercalated ZLG/SiC, $E_p = 60$ eV.

spectrum of the covered region (1) has no features apart from those associated with vibrations of the 6*H*-SiC crystal lattice.

However, several new features characteristic of graphene appeared in the high-frequency part of the spectrum measured in the central region of the sample: the D (~ 1350 cm^{-1}), G (~ 1585 cm^{-1}), $2D$ (~ 2700 cm^{-1}), $D + D'$ (~ 2930 cm^{-1}), and $2D'$ (~ 3200 cm^{-1}) Raman lines. Emergence of the double-resonance $2D$ and $2D'$ lines is an explicit sign of graphene film formation, since these features are related to the unique graphene band structure and phonon dispersion [69]. Typically, the G and $2D$ lines of single-layer epitaxial graphene grown on 6*H*-SiC (located at ~ 1600 and ~ 2720 cm^{-1}, respectively) are strongly blueshifted relative to their positions in exfoliated graphene [70]. The main reason for this shift is the compressive strain inherent in epitaxial graphene grown on 6*H*-SiC. In the sample under study, the G and $2D$ Raman lines (positioned at 1589 and 2700 cm^{-1}, respectively) have significantly lower blueshifts than those reported in Ref. [70]. This may indicate a lower level of strain in the graphene film, which confirms its quasi-freestanding character.

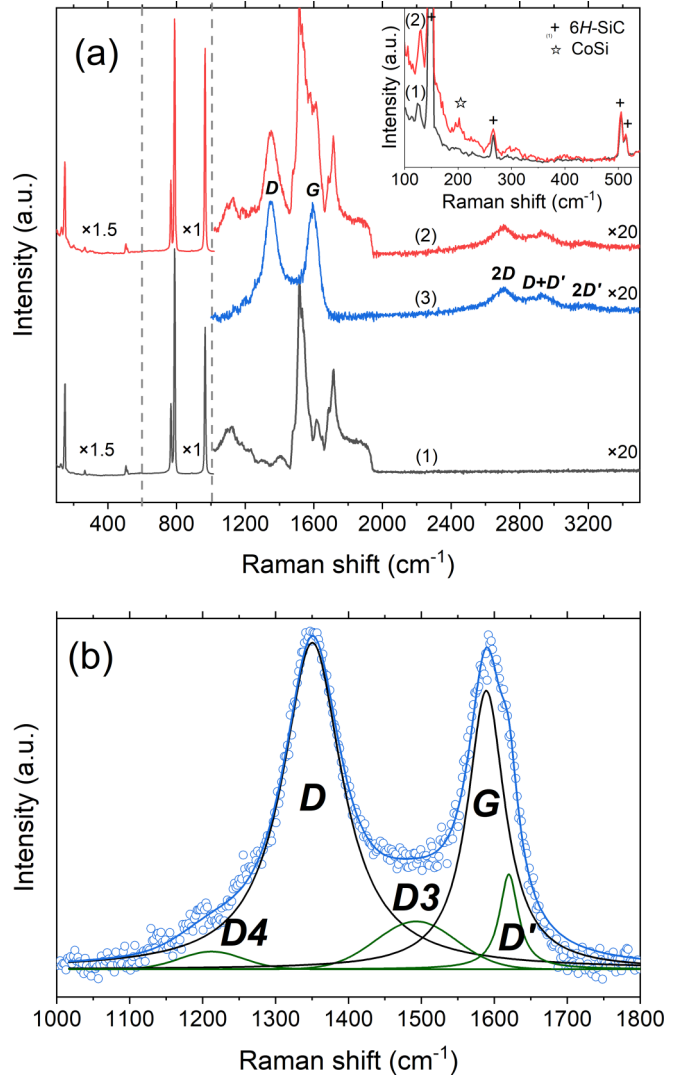The presence of the D and $D + D'$ lines in the spectrum point out the existence of defects in graphene film.

FIG. 9. (a) Raman spectra of the covered 6*H*-SiC substrate (1), spectrum of ZLG grown on 6*H*-SiC after Co intercalation (2), and the same spectrum in the 1000–3500 cm^{-1} frequency range upon subtraction of the substrate contribution (3). The intensities of the high-frequency and low-frequency parts of the spectra were increased for better visualization. Inset shows the comparison of the low-frequency parts of the spectra (1) and (2). (b) Spectrum (3) in the 1000–1800 cm^{-1} frequency range. Open circles demonstrate the experimental data, and solid lines represent the results of deconvolution.

Moreover, several lower-intensity defect-related lines can be distinguished in the 1000–1800 cm^{-1} frequency region. Deconvolution of the spectrum obtained from the central region of the sample onto five bands is presented in Fig. 9(b). The D and D' lines are due to the defect-related double-resonance Raman processes [69]. The $D3$ line (~ 1500 cm^{-1}) corresponds to the amorphous sp^2 carbon fraction in carbonaceous materials, and its intensity reflects the fraction of amorphous carbon in the crystal lattice [71]. The $D4$ (~ 1200 cm^{-1}) line is associated with the peak of the density of vibrational states in the phonon dispersion of graphite [72] and points to the presence of topological disorder in the graphite lattice [73–75].

The technique presented in Ref. [76] makes it possible to determine the degree of defectiveness of the graphene films and to establish the nature of defects. This technique consists in the simultaneous consideration of two parameters: the FWHM of the G line and the ratio of the integrated intensities of the D and G lines ($A(D)/A(G)$) multiplied by the fourth power of the used excitation wavelength. In our case, the FWHM of the G line is 62 cm^{-1}, and the value of the $A(D)/A(G)$ ratio is 1.86. According to the data of [76], such a combination of the parameters of the spectral lines indicates the dominance of linear defects in the crystal lattice of the sample, i.e., the polycrystallinity of the graphene film. The average crystallite size can be calculated using the following formula [77]:

$$L_a(\text{nm}) = (2.4 \times 10^{-10}) \lambda_l^4 (A(D)/A(G))^{-1}, \qquad (1)$$

where $\lambda_l = 532$ nm is the excitation light wavelength. Thus the average crystalline size is 10.3 nm according to Eq. (1).

The XPS data presented above (Fig. 5) indicate the presence of CoSi and CoSi$_2$ layers under graphene. The CoSi$_2$ layer does not give any detectable contribution to the Raman spectra, however, the CoSi layer demonstrates a rather strong line at 204 cm^{-1} and a weaker one at 224 cm^{-1} [78–80]. When comparing the low-frequency parts of the spectra [inset in Fig. 9(a)], one can notice the appearance of an additional line with a frequency of 204 cm^{-1} in the spectrum of the central region of the sample. This feature can be associated with CoSi, the most prominent line of which has the same frequency. Thus the Raman spectroscopy data confirm the conclusions drawn from the XPS data on the presence of cobalt silicides under the graphene film.

4. SQUID measurements and analysis

To study the magnetic properties of the sample, the SQUID measurements were carried out by applying the magnetic field parallel to the surface ($\perp c$ axis). It is known that for cobalt silicides on Si(100) the easy magnetization axis lies in the surface plane, while it is more difficult to magnetize in the out-of-plane direction [19]. CoSi compound, which is a diamagnet in the bulk [81], exhibits magnetic properties in nanoforms due to uncompensated spins of the surface Co atoms [82]. Whereas CoSi$_2$ does not have a strong magnetic properties in thin films of several nanometers thickness [83].

In Figs. 10(a) and 10(b), the magnetization curves $M(H)$ of Co-intercalated ZLG/SiC sample measured with in-plane field at various temperatures are presented. Figure 10(c) shows the change of hysteresis loop with the sample temperature. An open hysteresis loop and coercivity in the temperature range 2–100 K is revealed. The maximum value of the coercive force is 180 Oe at 2 K. This value decreases with the temperature increase, and the hysteresis loop is practically closed at room temperature. At the same time, the value of the saturation magnetization decreases with the temperature increase [Fig. 10(a)]. It is observed that the magnetization saturates at a high applied magnetic field of 40 kOe and for all temperatures. This indicates that all spins are ordered and align along the field direction at the high magnetic field.

Interestingly, the magnetization curves [Fig. 10(b)] have a two-jump loop shape [83–85]. This behavior is typical
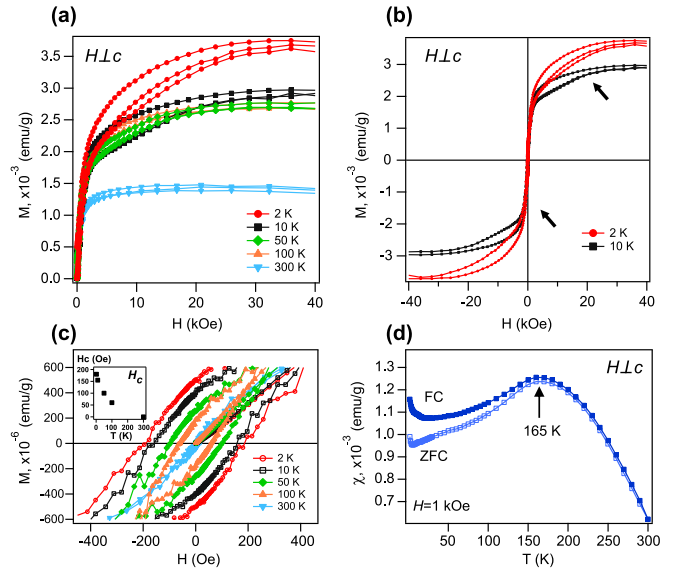

FIG. 10. (a) Isothermal magnetization curves $M(H)$ of Co-intercalated ZLG/SiC sample at various temperatures. (b) Two $M(H)$ curves at 2 and 10 K in full range of applied field to demonstrate the two-jump process of hysteresis loop. (c) Modification of hysteresis loops at different temperatures obtained from the $M(H)$ curves. Plot of coercive field (H_C) as a function of temperature is in the inset. (d) Temperature dependence of magnetic susceptibility $\chi(T)$ measured in the field $H = 1$ kOe. Zero-field-cooled (ZFC) curve is denoted by open symbols and field-cooled (FC) curve - by filled symbols.

for epitaxial ferromagnetic thin films with in-plane uniaxial anisotropy which influences on the cubic magnetocrystalline anisotropy. In this case, the change in magnetization strongly depends on the orientation of applied field. If the field is not coherent with one of the cubic easy axes and slightly tilted off the hard axis, the magnetization is more difficult and the two-jump process can be observed. The jumps are marked in Fig. 10(b) by black arrows on the curve upon cycling the field between negative and positive values. The two-jump loop shape is reproduced upon reverse cycling the field.

The temperature dependences of zero-field-cooled (ZFC) and field-cooled (FC) magnetic susceptibility $\chi(T)$ are shown in Fig. 10(d). The magnetic susceptibility $\chi(T)$ both in ZFC and FC curves has a broad maximum at ~165 K. It can be associated with superparamagnetism as was early shown in cobalt ferrite or iron-palladium alloy nanoparticles [86–88]. The ZFC and FC curves diverge noticeably below 165 K, and a slight divergence of the curves remains above this temperature up to 300 K. Similar behavior of magnetic susceptibility curves with presence of hysteresis loop has been reported for the CoSi nanowires study [82]. Both of ZFC and FC curves rise when temperature decreases below 5 K. This correlates with an increase in the saturation magnetization of $M(H)$ curve at 2 K [Fig. 10(a)]. Saturation magnetization slightly changes in the temperature range 10–100 K, but the coercive field gradually decreases with increasing temperature [Fig. 10(c)].

Therefore the system of graphene/CoSi/CoSi$_2$/SiC demostrates in-plane ferromagnetic properties with open

hysteresis loop and we suggest that nanothin layer of CoSi is responsible for the observed effect.

IV. CONCLUSION

In the present work, the synthesis parameters of zero-layer graphene (ZLG) on 6*H*-SiC(0001) were determined. We found that it is possible to synthesize ZLG by one-step high-temperature annealing of SiC at 1150 °C with preliminary degassing of the sample. The LEED, XPS and ARPES results prove the formation of ZLG with typical photoelectron spectra and diffraction pattern. The electronic structure of ZLG on SiC was investigated by ARPES in a wide range of binding energies and momenta. The DFT calculated band structure is consistent with ARPES intensity maps.

We study the two methods of Co deposition on ZLG/SiC: Co deposition on the heated substrate and Co deposition on the room-temperature substrate with subsequent annealing. We revealed that both methods lead to intercalation of Co and transformation of ZLG into a graphene monolayer. At the same time, Co deposition on the heated substrate is more effective for transformation of ZLG into graphene.

Synthesized graphene has a quasi-freestanding character while ultra-thin $CoSi/CoSi_2$ layers are formed underneath it. HRTEM and AFM results allowed to obtain informa-tion about the crystal structure of CoSi and $CoSi_2$ layers in detail. Based on magnetic measurements, we can conclude that graphene/$CoSi$/$CoSi_2$/SiC structure shows the ferromag-netic properties with an open hysteresis loop and magnetic coercivity.

In summary, we obtained the quasi-freestanding graphene in contact with magnetic substrate, while preserving Dirac-cone-like band structure. This conclusion is supported by DFT calculations. The outcomes are important for implementation of magneto-spin-orbit graphene on a semiconducting sub-strate and application of such graphene in spintronics devices.

[1] A. H. Castro Neto, F. Guinea, N. M. R. Peres, K. S. Novoselov, and A. K. Geim, Rev. Mod. Phys. **81**, 109 (2009).

[2] D. Pesin and A. H. MacDonald, Nat. Mater. **11**, 409 (2012).

[3] A. G. Rybkin, A. A. Rybkina, M. M. Otrokov, O. Y. Vilkov, I. I. Klimovskikh, A. E. Petukhov, M. V. Filianina, V. Y. Voroshnin, I. P. Rusinov, A. Ernst, A. Arnau, E. V. Chulkov, and A. M. Shikin, Nano Lett. **18**, 1564 (2018).

[4] A. A. Rybkina, A. G. Rybkin, I. I. Klimovskikh, P. N. Skirdkov, K. A. Zvezdin, A. K. Zvezdin, and A. M. Shikin, Nanotechnology **31**, 165201 (2020).

[5] A. M. Shikin, A. A. Rybkina, A. G. Rybkin, I. I. Klimovskikh, P. N. Skirdkov, K. A. Zvezdin, and A. K. Zvezdin, Appl. Phys. Lett. **105**, 042407 (2014).

[6] K. V. Emtsev, A. Bostwick, K. Horn, J. Jobst, G. L. Kellogg, L. Ley, J. L. McChesney, T. Ohta, S. A. Reshanov, J. Röhrl, E. Rotenberg, A. K. Schmid, D. Waldmann, H. B. Weber, and T. Seyller, Nat. Mater. **8**, 203 (2009).

[7] U. Starke and C. Riedl, J. Phys.: Condens. Matter **21**, 134016 (2009).

[8] T. Gao, T. Gao, C. Chang, Y. Chen, M. Liu, S. Xie, K. He, X. Ma, Y. Zhang, and Z. Liu, ACS Nano **6**, 6562 (2012).

[9] A. A. Gogina, A. G. Rybkin, A. M. Shikin, L. Petaccia, G. Di Santo, I. A. Eliseev, V. Y. Davydov, and I. I. Klimovskikh, JETP **132**, 906 (2021).

[10] G. S. Grebenyuk, I. A. Eliseev, S. P. Lebedev, E. Y. Lobanova, D. A. Smirnov, V. Y. Davydov, A. A. Lebedev, and I. I. Pronin, Phys. Solid State **62**, 519 (2020).

[11] Y. Zhang, H. Zhang, Y. Cai, J. Song, and P. He, Nanotechnology **28**, 075701 (2017).

[12] S. Wolff, S. Roscher, F. Timmermann, M. V. Daniel, F. Speck, M. Wanke, M. Albrecht, and T. Seyller, Ann. Phys. **531**, 1900199 (2019).

[13] K. V. Emtsev, A. A. Zakharov, C. Coletti, S. Forti, and U. Starke, Phys. Rev. B **84**, 125423 (2011).

[14] A. Stöhr, S. Forti, S. Link, A. A. Zakharov, K. Kern, U. Starke, and H. M. Benia, Phys. Rev. B **94**, 085431 (2016).

[15] S. Forti, A. Stöhr, A. A. Zakharov, C. Coletti, K. V. Emtsev, and U. Starke, 2D Mater. **3**, 035003 (2016).

[16] M. G. Silly, G. Li, and Y. J. Dappe, Surf. Interface Anal. **46**, 1273 (2014).

[17] R. Hönig, P. Roese, K. Shamout, T. Ohkochi, U. Berges, and C. Westphal, Nanotechnology **30**, 025702 (2019).

[18] J. S. Tsay, C. S. Yang, Y. Liou, and Y. D. Yao, J. Appl. Phys. **85**, 4967 (1999).

[19] K. Wang, Y. Zhao, G. Li, C. Wu, Q. Wang, and J. He, IEEE Trans. Magn. **51**, 1 (2015).

[20] H. Takenaka, S. Sandhoefner, A. A. Kovalev, and E. Y. Tsymbal, Phys. Rev. B **100**, 125156 (2019).

[21] Y. Zhou and F. Liu, Nano Lett. **21**, 230 (2021).

[22] G. H. Major, N. Fairley, P. M. A. Sherwood, M. R. Linford, J. Terry, V. Fernandez, and K. Artyushkova, J. Vac. Sci. Technol. A **38**, 061203 (2020).

[23] V. Jain, M. C. Biesinger, and M. R. Linford, Appl. Surf. Sci. **447**, 548 (2018).

[24] See Supplemental Materials at http://link.aps.org/supplemental/10.1103/PhysRevB.104.155423 for details of the XPS data analysis as well as additional ARPES data and DFT calculation results.

[25] P. M. T. M. van Attekum and G. K. Wertheim, Phys. Rev. Lett. **43**, 1896 (1979).

[26] D.-Q. Yang and E. Sacher, Langmuir **22**, 860 (2006).

[27] T. T. P. Cheung, J. Appl. Phys. **53**, 6857 (1982).

[28] A. Kovtun, D. Jones, S. Dell'Elce, E. Treossi, A. Liscio, and V. Palermo, Carbon **143**, 268 (2019).

[29] D. Cabrera-German, G. Gomez-Sosa, and A. Herrera-Gomez, Surf. Interface Anal. **48**, 252 (2016).

[30] T. Ozaki, Phys. Rev. B **67**, 155108 (2003).

[31] T. Ozaki and H. Kino, Phys. Rev. B **69**, 195113 (2004).

[32] J. P. Perdew, K. Burke, and M. Ernzerhof, Phys. Rev. Lett. **77**, 3865 (1996).

[33] T. Cavallucci and V. Tozzini, J. Phys. Chem. C **120**, 7670 (2016).

[34] P. A. Denis, C. Pereyra Huelmo, and F. Iribarne, New J. Chem. **43**, 11251 (2019).

[35] C.-C. Lee, Y. Yamada-Takamura, and T. Ozaki, J. Phys.: Condens. Matter **25**, 345501 (2013).

[36] G. K. H. Madsen, P. Blaha, K. Schwarz, E. Sjöstedt, and L. Nordström, Phys. Rev. B **64**, 195134 (2001).

[37] P. Blaha, K. Schwarz, F. Tran, R. Laskowski, G. K. H. Madsen, and L. D. Marks, J. Chem. Phys. **152**, 074101 (2020).

[38] K. V. Emtsev, F. Speck, T. Seyller, L. Ley, and J. D. Riley, Phys. Rev. B **77**, 155303 (2008).

[39] C. Riedl, C. Coletti, and U. Starke, J. Phys. D **43**, 374009 (2010).

[40] C. Riedl, U. Starke, J. Bernhardt, M. Franke, and K. Heinz, Phys. Rev. B **76**, 245406 (2007).

[41] P. Merino, Ph.D. thesis, Universidad Autónoma de Madrid, 2014.

[42] C. Riedl, C. Coletti, T. Iwasaki, A. A. Zakharov, and U. Starke, Phys. Rev. Lett. **103**, 246804 (2009).

[43] P. Mårtensson, F. Owman, and L. I. Johansson, Phys. Status Solidi (b) **202**, 501 (1997).

[44] K. Emtsev, Ph.D. thesis, Friedrich-Alexander-Universität Erlangen-Nürnberg, 2009.

[45] F. Varchon, R. Feng, J. Hass, X. Li, B. N. Nguyen, C. Naud, P. Mallet, J.-Y. Veuillen, C. Berger, E. H. Conrad, and L. Magaud, Phys. Rev. Lett. **99**, 126805 (2007).

[46] J. Wang, M. Kim, L. Chen, K.-M. Ho, M. Tringides, C.-Z. Wang, and S. Wang, Phys. Rev. B **103**, 085403 (2021).

[47] G. S. Grebenyuk, E. Y. Lobanova, D. A. Smirnov, I. A. Eliseev, A. V. Zubov, A. N. Smirnov, S. P. Lebedev, V. Y. Davydov, A. A. Lebedev, and I. I. Pronin, Phys. Solid State **61**, 1316 (2019).

[48] L. I. Johansson, F. Owman, and P. Mårtensson, Phys. Rev. B **53**, 13793 (1996).

[49] R. Hönig, Ph.D. thesis, Technischen Universität Dortmund, 2019.

[50] M. García-Méndez, F. Castillón, G. Hirata, M. Farías, and G. Beamson, Appl. Surf. Sci. **161**, 61 (2000).

[51] J. Nam, I. Y. Hwang, J. H. Kim, H. J. Kang, Y. H. Ha, D. W. Moon, D. J. O'connor, and R. J. Macdonald, J. Korean Phys. Soc. **35**, 546 (1999).

[52] J. Zhao and D. M. Poirier, Surf. Sci. Spectra **7**, 322 (2000).

[53] J. L. Tedesco, J. E. Rowe, and R. J. Nemanich, J. Appl. Phys. **105**, 083721 (2009).

[54] A. G. Rybkin, A. A. Rybkina, A. V. Tarasov, D. A. Pudikov, I. I. Klimovskikh, O. Y. Vilkov, A. E. Petukhov, D. Y. Usachov, D. A. Estyunin, V. Y. Voroshnin, A. Varykhalov, G. Di Santo, L. Petaccia, E. F. Schwier, K. Shimada, A. Kimura, and A. M. Shikin, Appl. Surf. Sci. **526**, 146687 (2020).

[55] A. Appelbaum, R. V. Knoell, and S. P. Murarka, J. Appl. Phys. **57**, 1880 (1985).

[56] V. Kotlyar, A. Alekseev, D. Olyanich, T. Utas, A. Zotov, and A. Saranin, Surf. Sci. **662**, 6 (2017).

[57] C. M. Comrie, H. Ahmed, D. Smeets, J. Demeulemeester, S. Turner, G. Van Tendeloo, C. Detavernier, and A. Vantomme, J. Appl. Phys. **113**, 234902 (2013).

[58] A. H. van Ommen, C. W. T. Bulle-Lieuwma, and C. Langereis, J. Appl. Phys. **64**, 2706 (1988).

[59] S. Doğan, D. Johnstone, F. Yun, S. Sabuktagin, J. Leach, A. A. Baski, H. Morkoç, G. Li, and B. Ganguly, Appl. Phys. Lett. **85**, 1547 (2004).

[60] S. Lin, Z. Chen, Y. Yang, S. Liu, Y. Ba, L. Li, and C. Yang, CrystEngComm **14**, 1588 (2012).

[61] M. Dudley, X. R. Huang, W. Huang, A. Powell, S. Wang, P. Neudeck, and M. Skowronski, Appl. Phys. Lett. **75**, 784 (1999).

[62] E. Emorhokpor, T. Kerr, I. Zwieback, W. Elkington, M. Dudley, T. Anderson, and J. Chen, MRS Proc. **815**, J5.19 (2004).

[63] M. Mucha-Kruczyński, O. Tsyplyatyev, A. Grishin, E. McCann, V. I. Fal'ko, A. Bostwick, and E. Rotenberg, Phys. Rev. B **77**, 195403 (2008).

[64] A. Bostwick, T. Ohta, J. L. McChesney, K. V. Emtsev, T. Seyller, K. Horn, and E. Rotenberg, New J. Phys. **9**, 385 (2007).

[65] D. Y. Usachov, A. V. Fedorov, O. Y. Vilkov, I. I. Ogorodnikov, M. V. Kuznetsov, A. Grüneis, C. Laubschat, and D. V. Vyalikh, Phys. Rev. B **97**, 085132 (2018).

[66] O. Vilkov, A. Fedorov, D. Usachov, L. V. Yashina, A. V. Generalov, K. Borygina, N. I. Verbitskiy, A. Grüneis, and D. V. Vyalikh, Sci. Rep. **3**, 2168 (2013).

[67] Z. J. Pan, L. T. Zhang, and J. S. Wu, J. Appl. Phys. **101**, 033715 (2007).

[68] C. Pirri, J. C. Peruchetti, G. Gewinner, and D. Bolmont, Solid State Commun. **57**, 361 (1986).

[69] A. C. Ferrari and D. M. Basko, Nat. Nanotechnol. **8**, 235 (2013).

[70] V. Y. Davydov, D. Y. Usachov, S. P. Lebedev, A. N. Smirnov, V. S. Levitskii, I. A. Eliseyev, P. A. Alekseev, M. S. Dunaevskiy, O. Y. Vilkov, A. G. Rybkin et al., Semiconductors **51**, 1072 (2017).

[71] M. Pawlyta, J.-N. Rouzaud, and S. Duber, Carbon **84**, 479 (2015).

[72] M. Couzi, J.-L. Bruneel, D. Talaga, and L. Bokobza, Carbon **107**, 388 (2016).

[73] A. C. Ferrari and J. Robertson, Philos. Trans. R. Soc. London, A **362**, 2269 (2004).

[74] K. C. Le, C. Lefumeux, P.-E. Bengtsson, and T. Pino, Proc. Combust. Inst. **37**, 869 (2019).

[75] B. Dippel, H. Jander, and J. Heintzenberg, Phys. Chem. Chem. Phys. **1**, 4707 (1999).

[76] L. G. Cançado, M. G. Da Silva, E. H. M. Ferreira, F. Hof, K. Kampioti, K. Huang, A. Pénicaud, C. A. Achete, R. B. Capaz, and A. Jorio, 2D Mater. **4**, 025039 (2017).

[77] L. G. Cançado, K. Takai, T. Enoki, M. Endo, Y. A. Kim, H. Mizusaki, A. Jorio, L. N. Coelho, R. Magalhaes-Paniago, and M. A. Pimenta, Appl. Phys. Lett. **88**, 163106 (2006).

[78] A. Perez-Rodriguez, E. Roca, T. Jawhari, J. R. Morante, and R. J. Schreutelkamp, Thin Solid Films **251**, 45 (1994).

[79] F.-M. Liu, B. Ren, Y.-X. Jiang, J.-H. Ye, and Z.-Q. Tian, Chem. Phys. Lett. **372**, 15 (2003).

[80] F. M. Liu, J. H. Ye, B. Ren, Z. L. Yang, Y. Y. Liao, A. See, L. Chan, and Z. Q. Tian, Thin Solid Films **471**, 257 (2005).

[81] V. N. Narozhnyi and V. N. Krasnorussky, J. Exp. Theor. Phys. **116**, 780 (2013).

[82] K. Seo, K. S. K. Varadwaj, P. Mohanty, S. Lee, Y. Jo, M.-H. Jung, J. Kim, and B. Kim, Nano Lett. **7**, 1240 (2007).

[83] B. Hu, W. He, J. Ye, J. Tang, S. A. Syed, X.-Q. Zhang, and Z.-H. Cheng, Chin. Phys. B **24**, 017502 (2015).

[84] C. Daboo, R. J. Hicken, E. Gu, M. Gester, S. J. Gray, D. E. P. Eley, E. Ahmad, J. A. C. Bland, R. Ploessl, and J. N. Chapman, Phys. Rev. B **51**, 15964 (1995).

[85] R. P. Cowburn, S. J. Gray, J. Ferré, J. A. C. Bland, and J. Miltat, J. Appl. Phys. **78**, 7210 (1995).

[86] C. Liu, A. J. Rondinone, and Z. J. Zhang, Pure Appl. Chem. **72**, 37 (2000).

[87] V. H. Ojha and K. M. Kant, J. Phys. Chem. Solids **148**, 109655 (2021).

[88] R. Nazir, M. Mazhar, M. J. Akhtar, M. R. Shah, N. A. Khan, M. Nadeem, M. Siddique, M. Mehmood, and N. M. Butt, Nanotechnology **19**, 185608 (2008).